Unraveling secondary ice production in winter orographic clouds through a synergy of in-situ observations, remote sensing and modeling

Paraskevi Georgakaki
Laboratory of Atmospheric Processes and their Impacts (LAPI), School of Architecture, Civil & Environmental Engineering, Ecole Polytechnique Fédérale de Lausanne, Lausanne, Switzerland.
https://orcid.org/0000-0002-4296-8779

Anne-Claire Billault-Roux
Environmental Remote Sensing Laboratory (LTE), School of Architecture, Civil & Environmental Engineering, Ecole Polytechnique Fédérale de Lausanne, Lausanne, Switzerland.

Romanos Foskinis
Laser Remote Sensing Unit (LRSU), Physics Department, National Technical University of Athens, Zografou, Greece; Center for Studies of Air Quality and Climate Change, Institute of Chemical Engineering Sciences, Foundation for Research and Technology Hellas, Patras, Greece; Environmental Radioactivity & Aerosol technology for atmospheric & Climate impacT Lab (ENRACT), Institute of Nuclear and Radiological Sciences and Technology, Energy and Safety, National Centre of Scientific Research “Demokritos”, Ag. Paraskevi, Greece; Laboratory of Atmospheric Processes and their Impacts (LAPI), School of Architecture, Civil & Environmental Engineering, Ecole Polytechnique Fédérale de Lausanne, Lausanne, Switzerland.

Kunfeng Gao
Laboratory of Atmospheric Processes and their Impacts (LAPI), School of Architecture, Civil & Environmental Engineering, Ecole Polytechnique Fédérale de Lausanne, Lausanne, Switzerland.
https://orcid.org/0000-0001-9482-3857

Georgia Sotiropoulou
Division of Environmental Physics and Meteorology, Department of Physics, University of Athens, Athens, Greece; Laboratory of Atmospheric Processes and their Impacts (LAPI), School of Architecture, Civil & Environmental Engineering, Ecole Polytechnique Fédérale de Lausanne, Lausanne, Switzerland.

Maria Gini
Environmental Radioactivity & Aerosol technology for atmospheric & Climate impacT Lab (ENRACT), Institute of Nuclear and Radiological Sciences and Technology, Energy and Safety, National Centre of Scientific Research “Demokritos”, Ag. Paraskevi, Greece.

Satoshi Takahama
Laboratory of Atmospheric Processes and their Impacts (LAPI), School of Architecture, Civil & Environmental Engineering, Ecole Polytechnique Fédérale de Lausanne, Lausanne, Switzerland.

Konstantinos Eleftheriadis

Environmental Radioactivity & Aerosol technology for atmospheric & Climate impacT Lab (ENRACT), Institute of Nuclear and Radiological Sciences and Technology, Energy and Safety, National Centre of Scientific Research “Demokritos”, Ag. Paraskevi, Greece https://orcid.org/0000-0003-2265-4905

Alexandros Papayannis

Laser Remote Sensing Unit (LRSU), Physics Department, National Technical University of Athens, Zografou, Greece; Laboratory of Atmospheric Processes and their Impacts (LAPI), School of Architecture, Civil & Environmental Engineering, Ecole Polytechnique Fédérale de Lausanne, Lausanne, Switzerland.

Alexis Berne

Environmental Remote Sensing Laboratory (LTE), School of Architecture, Civil & Environmental Engineering, Ecole Polytechnique Fédérale de Lausanne, Lausanne, Switzerland https://orcid.org/0000-0003-4977-1204

Athanasios Nenes (athanasios.nenes@epfl.ch)

Laboratory of Atmospheric Processes and their Impacts (LAPI), School of Architecture, Civil & Environmental Engineering, Ecole Polytechnique Fédérale de Lausanne, Lausanne, Switzerland; Center for Studies of Air Quality and Climate Change, Institute of Chemical Engineering Sciences, Foundation for Research and Technology Hellas, Patras, Greece.

Article

Keywords:

Posted Date: November 9th, 2023

DOI: https://doi.org/10.21203/rs.3.rs-3502790/v1

Additional Declarations: (Not answered)

Abstract

Recent years have shown that secondary ice production (SIP) is ubiquitous, affecting all clouds from polar to tropical regions. SIP is not described well in models and for this may vastly underpredict ice crystal number concentrations in warm mixed-phase clouds. Through a synergy of modeling, remote sensing and in-situ measurements carried out in an orographic environment during the Cloud-AerosoL InteractionS in the Helmos background TropOsphere (CALISHTO) campaign, we show that SIP can have a profound impact on the vertical distribution of hydrometeors and precipitation, especially in seeder-feeder configurations which are encountered in multi-layered cloud systems. The mesoscale model simulations coupled with a radar simulator strongly support a unique signature that is characteristic of SIP; because of this, our study opens the possibility of using the vast global archive of cloud radar data for systematically inferring SIP signatures and frequency of occurrence.

INTRODUCTION

The distribution of the ice and liquid phases of water within mixed-phase clouds (MPCs) significantly affects surface cloud radiative forcing [1,2] and the hydrological cycle[3,4]. MPCs exhibit spatial heterogeneity at spatial scales lower than 100 m, with spatially separated ice- and liquid-phase clusters [5–7]. This heterogeneity impacts the efficiency of the Wegener-Bergeron-Findeisen (WBF) process [8–10] (where ice crystals grow at the expense of cloud droplets) and the rate of cloud glaciation. Accurately representing these processes in numerical weather prediction (NWP) and climate models remains a major challenge and a source of model bias[11–13].

Ice crystal number concentration (ICNC) in mixed phase clouds is expected to be modulated by the availability of ice nucleating particles (INPs) [14,15]. The sparsity of INPs [16,17] at temperatures above -20°C cannot account for ICNCs observed in MPCs. Secondary ice production (SIP) following the initial primary ice nucleation events must be considered to bridge the gap between the limited availability of INPs and the abundance of ICNCs [18,19]. Atmospheric models neglecting the effect of SIP are therefore prone to underestimate simulated ICNCs at warm subzero temperatures with important implications for the radiative properties and microphysical evolution of this type of clouds [20–22].

The importance of SIP has been widely acknowledged in laboratory [23–26], field [27–29], remote sensing [30–33], and modeling studies [34–36] worldwide [37]. The most commonly invoked SIP processes include the Hallett-Mossop (HM) or rime-splintering process [38,39], ice-ice collisional break-up (BR) [40,41], and droplet-shattering during freezing (DS) [42,43]. While HM is extensively incorporated in atmospheric models, its efficiency is limited to a narrow temperature range of -8°C to -3°C and specific cloud microphysical configurations. Recent experimental studies even suggest potential overestimation of the efficiency of this process [44]. Vigorous convective downdrafts [45,46] and associated subsaturated regions may also foster the break-up of graupel and dendritic snow particles from sublimation (SUBBR) [47,50].

A major challenge is the ability to detect the presence of SIP in global MPCs, ideally with insights on its intensity and mechanisms. Without such information, models lack a key microphysical constraint that impedes progress in the description of MPCs. Ground-based remote sensing observations of cloud and precipitation can provide key information for constraining SIP [48,49,32,33]. One approach is to use lidar and radar retrievals to extract ice multiplication factors (i.e., ICNCs/INPs); application of such a method in wintertime orographic MPCs indicated the widespread occurrence of SIP, with a frequency exceeding 85% [50]. Doppler spectra from vertically-pointing radars provide another powerful approach, as they often exhibit multimodal distributions within the temperature range associated with SIP or within the dendritic growth layer (DGL), typically between -20 and -10°C [51]. These distributions suggest interactions between fast-falling and slower-falling particles within the radar volume from riming [52] or new ice formation [30,32,49,53]. Significant ambiguity however remains on the interpretation of these signals, as downdrafts, horizontal winds, turbulence or other measurement uncertainties can affect their interpretation.

Here, we show – by coupling high-resolution predictive modeling with a forward radar simulator [54–56] – that characteristic signatures in observed cloud radar data can indeed be attributed to the presence of SIP, as inclusion of the latter significantly improves the agreement with the radar observations, including the vertical distribution of precipitation and the timing thereof, and thus opening the possibility to leverage the abundant cloud remote sensing observations for SIP signatures.

RESULTS

We employed a version of the mesoscale Weather Research and Forecasting (WRF) model, which incorporates detailed descriptions of SIP processes, to investigate the microphysics driving an intense snowfall event observed on December 18, 2021 in mainland Greece. Doppler spectrograms along with timeseries of radar moments were captured by a W-band spectral zenith profiler (WProf) [57], deployed at Mount Helmos in Peloponnese, as part of the Cloud-AerosoL InteractionS in the Helmos background TropOsphere (CALISHTO) campaign (https://calishto.panacea-ri.gr/). The radar observations provided valuable insights into the microphysics of snowfall and served as a basis for evaluating the performance of the WRF model and investigating potential SIP signatures.

Comparing radar observations with radar observables

Figure 1 shows time-height contours of two standardized moments of the Doppler spectra measured by WProf: reflectivity (Fig. 1a) and skewness (Fig. 1e). WProf was deployed at the “Vathia Lakka” (VL) station, located on the lee-side of the mountain-top station, Helmos Hellenic Atmospheric Aerosol and Climate Change (HAC)[2] [58], at an elevation of approximately 1850 m above mean sea level (AMSL). The measured reflectivity primarily reflects variations in hydrometeor size and total concentration, while skewness provides insight into the spectral asymmetry. A low-pressure system associated with the passage of storm Carmel reached the CALISHTO measurement sites on the evening of December 17, 2021. The radar timeseries reveals three distinct cloud periods indicated by the turquoise boxes shown in

Fig. 1a. The distinction between these three cloud periods in both measurements and simulations is based on the presence of seeding ice particles falling either from higher levels within the same cloud (internal seeding) or from an overlying cloud (external seeder-feeder), as summarized in Supplementary Fig. 1.

The first cloud system exhibits a characteristic nimbostratus cloud structure, while the second one appears in a distinctive seeder-feeder cloud configuration, which is frequently observed in orographic environments [59]. Upon advection of the seeder cloud, a low-level orographic cloud persisted for almost one day. The skewness timeseries reveal the presence of extended regions with positive or negative signs especially during the first two cloud periods (Fig. 1e). Changes in the sign of skewness imply changes in the balance of the different hydrometeor populations within the radar volume. With the sign convention employed here, negative skewness means that the Doppler spectra are skewed towards the more massive, faster-falling side.

To evaluate the simulations and understand the cloud microphysical processes occurring in the radar volume, we configured the Cloud Resolving Model Radar Simulator (CR-SIM) [54] to replicate the characteristics of WProf and coupled it with the outputs from the WRF grid cell nearest to the VL station. Three sensitivity experiments were performed with WRF (see methods): CONTROL and DEMOTT account only for primary ice production (PIP). The former follows the temperature-dependent PIP descriptions included in the default version of WRF, while the latter was updated with the more advanced aerosol-aware scheme developed by Demott [60]. ALLSIP simulation employs the aerosol-dependent scheme used in DEMOTT and further considers the action of four SIP processes, namely HM, BR, DS and SUBBR.

The comparison between radar measurements and WRF simulations focuses solely on the radar equivalent reflectivity factor (Ze_w) (Fig. 1a-d), since the other radar observables were less accurately simulated by CR-SIM (not shown). Replacing the default PIP scheme of WRF used in CONTROL (Fig. 1b) with the aerosol-aware scheme in DEMOTT (Fig. 1c), leads to a notable reduction in predicted Ze_w values across all altitudes, especially at temperatures below -20°C. The activation of SIP mechanisms within the model induces a distinct shift in simulated Ze_w towards higher values, primarily within the DGL temperature zone (Fig. 1d), which becomes more pronounced during the initial two cloud periods. Evaluation of the simulations against the radiometer-derived liquid water path (LWP) is also provided in Fig. 1f. Over the simulation period, there is a substantial but highly variable amount of LWP present. Although the simulations tend to overestimate the radiometer-derived LWP measured at VL, they capture the timing of the peaks in the LWP timeseries, with ALLSIP more effectively reducing the simulated LWP, bringing it closer to observations.

Despite the good performance of WRF, the timing of the first two cloud events does not perfectly align with the remote sensing observations (Figs. 1a-d). Coupling CR-SIM with the grid cells surrounding the one closer to VL, or substituting the ERA5 reanalysis forcing dataset with the National Centers for Environmental Prediction (NCEP) dataset did not improve the simulated timing of either cloud events (not shown). The most plausible explanation for this discrepancy may be errors in predicted wind fields and

relative humidity with respect to ice (RH_i; Supplementary Fig. 2b). Further evaluation of the model at higher altitudes is impeded by the intense snowfall during storm Carmel, which prevented the derivation of the wind profile from the wind lidar deployed at VL. Despite these model-observation discrepancies, WRF coupled with CR-SIM can sufficiently capture the presence of the three consecutive cloud systems measured at VL, which is remarkable given the complex microphysics and small-scale turbulent flow over such complex orographic terrain (Supplementary Fig. 3b). A statistical summary of Ze_w for each cloud period is provided in Figs. 4b, 5b and Supplementary Fig. 4, that will help us uncover which WRF model configuration results in predictions that align most closely with the WProf measurements. Before delving into this comparison, it is essential to gain a better understanding of the microphysical processes that shape the simulated ice- and liquid-phase partitioning, and subsequently, the Ze_w values generated by the three WRF sensitivity simulations.

Microphysical process insights

Figure 2 illustrates the temporal evolution of vertical profiles for the total ICNC (cloud ice + snow + graupel), while Fig. 3 presents the corresponding profiles for the total liquid water content (LWC), as predicted by the three sensitivity simulations of WRF. These profiles – extracted from the WRF grid point nearest to the VL station (i.e., the same location used for running the CR-SIM simulator) – provide insights into the sources and sinks of ice and liquid hydrometeors driving the vertical distribution of Ze_w.

The hatched region in Fig. 2a delineates where water vapor is supersaturated with respect to ice (according to the CONTROL simulation). During the first cloud period, frozen hydrometeors precipitate from the higher-level parts of the cloud, without experiencing ice subsaturation before entering the low-level MPC below ~1 km. In contrast, during the external seeder-feeder period, subsaturated air separates the orographic cloud from the synoptic cloud above. Accurate representation of the microphysical processes underlying such multi-layered cloud systems in NWP models is found to be crucial for correctly simulating the cloud glaciation fraction as well as the amount of orographic precipitation [61,62].

Within the first two seeding cloud periods, falling ice particles undergo effective mass gain, initially through vapor deposition, in the ice supersaturated cloud regions (Fig. 3) at temperatures below -20°C. As a result, these particles vary in size and experience different terminal velocities, enhancing their collision efficiencies and facilitating further growth through aggregation (Fig. 2). Ice crystal growth through riming is also prevalent in the lower atmospheric levels of CONTROL (Fig. 3a), but is found to contribute even at colder temperatures in DEMOTT and ALLSIP, where higher-level clouds are not entirely glaciated (Figs. 4b, c). The role of INP description between simulations also carries important implications for the LWC and ICNCs at cold temperatures (see Supplementary Text 1).

Activation of SIP in the ALLSIP simulation shifts the yellowish shades (indicative of higher ICNCs) that were observed predominantly at temperatures below -20°C in CONTROL, towards the warmer temperature range between -20 and -10°C (Fig. 2c). This leads to a reduction in the vertical availability of LWC, which is noticeable especially during the nimbostratus period (Fig. 3c). The colored contours in Fig. 2c delineate

the regions where significant ice particle production occurs due to various SIP processes included in WRF. It is evident that SIP is particularly efficient during the first two seeding events, with limited and localized contributions from DS during the third cloud period (Fig. 2c). By examining the characteristic sizes of raindrops in M05, we find that they rarely exceed the threshold of 50 μm required for DS activation (Supplementary Fig. 5b). This explains the occurrence of spikes in the contours of DS production rates in the timeseries presented in Fig. 2c. SUBBR also shows highly localized effects when precipitating ice particles fall through subsaturated air layers (Supplementary Fig. 6). The HM process remains completely inactive during the simulation period, partially due to the colder temperatures at which the simulated clouds are formed, and also because the imposed ice and liquid thresholds are not met (see methods).

BR demonstrates significant particle production rates, exceeding 10^{-3} particles $L^{-1}s^{-1}$ at temperatures below the DGL, with a tenfold increase in efficiency within this temperature range (Fig. 2c). This substantial enhancement in BR rates, by two to three orders of magnitude compared to SUBBR and DS, suggests the predominance of the BR mechanism in the simulated cloud systems. Another noteworthy observation is that the snowflake aggregation contours (Supplementary Fig. 6) consistently envelop the BR contours (Fig. 2c). In particular, inside the DGL, collisions of aggregated dendrites can trigger SIP through BR. Although the ice habit is not explicitly resolved in M05, the number of fragments described by the employed Phillips [63] BR parameterization shows a triangular relationship with temperature, peaking at around -15°C, which justifies the peak in its efficiency inside the DGL.

The simultaneous enhancement of aggregation and new ice particle formation through BR is consistently highlighted in several modeling [62,64] and remote sensing studies [51]. Images of fragmented dendritic crystals captured during aircraft flights within nimbostratus clouds over China revealed the predominance of SIP via BR, particularly between -10°C and -15°C [65]. Importantly, during the 3rd cloud period, when aggregation is not favored in ALLSIP (Supplementary Fig. 6), SIP through BR is entirely inefficient.

SIP indications in Doppler spectra

Integrating information from the high-resolution modeling framework and radar Doppler spectra, allows for attributing distinct radar signals to SIP or other microphysical processes. This is done by comparing the simulated Ze_w for all three sensitivity simulations of WRF examined in this study. The unavailability of polarimetric radar observables during the CALISHTO campaign restricts our ability to identify specific ice hydrometeor habits (i.e., columnar crystals), which have proven valuable in previous research [30,53]. Nonetheless, we will focus on two specific moments of the timeseries – one from the nimbostratus and the other from the seeder-feeder cloud periods, as these periods were identified to create favorable conditions for SIP.

Starting from the nimbostratus cloud period, Fig. 4a presents an example Doppler spectrogram (Fig. 4a) measured by the WProf on December 18 at 03:55:10 UTC. Analyzing radar Doppler spectra, particularly in the presence of multimodes/peaks, helps reveal distinct hydrometeor populations within the same radar volume. The chosen spectrogram highlights a turbulent region between 2-2.5 km altitude, below which a

clear bimodal distribution appears at around 1.6 km, signifying two hydrometeor populations. Median statistics derived for this cloud period are summarized in Fig. 4b. The gray shaded regions in this plot indicate the observed interquartile range (IQR). CONTROL overestimates Ze_w at temperatures ranging from roughly -25°C to -17°C, while underestimates Ze_w at warmer subzero temperatures. The updated PIP scheme in DEMOTT agrees better with observations at temperatures colder than ∼-18°C, but still fails to achieve the higher Ze_w values observed at warmer temperatures. In contrast, ALLSIP enhances the simulated Ze_w by over 10 dBZ at these temperatures, reducing the discrepancy with the WProf measurements. Analysis of simulated ice particle size distributions (Supplementary Fig. 7) reveals that, closer to the ground (∼700 m AGL), ALLSIP predicts more than two (one) orders of magnitude elevated ICNCs compared to CONTROL (DEMOTT). In terms of large particles dominating the radar reflectivity, ALLSIP predicts tenfold higher snow particle concentrations compared to the other two sensitivity simulations (Supplementary Fig. 7e), likely from increased cloud-ice-to-snow autoconversion. However, at colder temperatures, particularly below -20°C, ALLSIP simulates lower snow and graupel concentrations relative to the WRF simulations disregarding SIP, resulting in Ze_w values below the observed IQR.

Despite uncertainties and simplifications in the modeling approaches (some further discussed in Supplementary Text 2), it becomes evident that, inside the DGL, inclusion of SIP mechanisms within ice seeding configurations is necessary for refining the vertical distribution of Ze_w, particularly the Ze_w enhancement near the ground. This implies that the ALLSIP simulation of WRF can be used to assess when characteristic radar signatures can be used to identify SIP processes.

Figure 4c illustrates the median tendency profiles for several microphysical processes simulated by ALLSIP within a 10-min timeframe of the observed WProf spectrogram (Fig. 4a). Ice particles grow through vapor deposition and aggregation while falling through the atmosphere. The primary mode detected by the cloud radar could therefore be attributed to dendritic and/or aggregated ice particles. Furthermore, the mean Doppler velocity (MDV) of the primary peak reaches up to ~ -2.5 m s^{-1} at 1 km altitude (Fig. 4a), which is significantly higher than the typical terminal velocities of aggregates at around 1 ms^{-1} [66]. Although large MDV could be caused by heavily rimed ice structures – WRF simulations do not suggest the presence of SLW (Fig. 3c). The high MDV is likely from the influence of downdrafts, and the effects of prevailing high horizontal winds (Supplementary Fig. 2c) and potential deviations in the vertical radar setup alignment [67].

Just above the -18°C isotherm, a secondary mode emerges in the radar Doppler spectrogram with a reflectivity of -0.4 dBZ (Fig. 4a). The pronounced reflectivity of the peak, alongside its broad spectral range, rules out the possibility of its origin being supercooled liquid droplets, as such droplets typically exhibit lower values below -15 dBZ [52]. Here it is worth noting that a single Doppler spectrogram at a specific timestep does not necessarily reflect the microphysical trajectory of a particle population [52]. The fast-falling spectral mode in Fig. 4a may, indeed, result from overlapping particle trajectories as they are advected toward the measurement site. To understand the origin of the secondary mode, we refer to the ALLSIP predictions (Fig. 4c). Simulated microphysical tendencies suggest that interactions between

particles of the primary mode entering the DGL may fuel SIP below 1.5 km altitude. Indeed, the emergence of the secondary mode in the Doppler spectrogram almost coincides with enhanced aggregation and BR in the model, the former peaking below -18°C. Efficient growth of sedimenting ice particles inside the DGL promotes differential settling, increasing the likelihood of collisions, which in turn drives both aggregation and BR. These two processes exhibit consistent alignment across all altitudes in the atmosphere. While snowflake aggregation can be an efficient ICNC sink in MPCs, Fig. 4c reveals that aggregation drives SIP through BR, which in turn compensates for the depletion of ice crystals and may even enhance them. Below ∼600 m, the source of ice particles due to BR can be up to one order of magnitude enhanced compared to the loss due to aggregation. At this altitude, interaction with supercooled droplets further augments ice crystal mass via riming (Fig. 4c). Riming and possibly WBF deplete cloud liquid water in lower atmospheric levels, improving agreement with radiometer-derived LWP compared to CONTROL and DEMOTT (Fig. 1f). The distinct spectral modes broaden and converge below ∼1 km, indicating an “advection-type” effect (although this could also relate to atmospheric turbulence or the imperfect vertical beam alignment during this instance).

Another important realization comes from reexamining the skewness timeseries, depicted in Fig. 1e. We observe that the emergence of the slower spectral mode coincides precisely with a region in the radar data showing persistent positive skewness, both temporally and spatially extended. This pattern bears similarity to findings in von Terzi [51], where a winter frontal case study unveiled spectral asymmetry associated with the rapid increase in Doppler spectral skewness at temperatures above -18°C. This was attributed to the formation of new small ice particles, likely due to SIP processes within the DGL. Giangrande [68] also linked bimodal spectra skewing toward slower falling particles with the formation and growth of ice needles. In our study, during the nimbostratus cloud period, persistent small ice particle formation is evident, represented by the red shading, at altitudes ranging from the -10 to -20°C isotherms after approximately 03:00 UTC on December 18 (Fig. 1e). This confirms that the observed bimodal spectrogram (Fig. 4a), although representing a single timestep, is not an isolated feature. The model with advanced SIP descriptions predicts enhanced BR (Fig. 2c) and aggregation (Supplementary Fig. 6) that aligns remarkably spatially and temporally with the increase in the observed spectral skewness (Fig. 1e). This one-to-one comparison allowed us to infer the presence of SIP through BR, resulting from collisions between delicate dendritic and/or aggregated ice structures inside the DGL, leading to a skewing of the Doppler spectra towards slower falling particles.

Moving to the seeder-feeder cloud period, Fig. 5 presents a WProf spectrogram juxtaposed with the corresponding vertical profiles of the WRF simulations. We discern the primary spectral mode corresponding to the aggregate population falling from the seeder cloud. A clear secondary mode becomes evident in the feeder cloud below the -16°C isotherm (Fig. 5a) – a region where the ALLSIP simulation suggests again the presence of SIP-generated particles (Fig. 5c). A high reflectivity of -1.0 dBZ together with its quite wide spectral signature indicate that the slow-falling spectral subpeak corresponds to cloud ice particles rather than supercooled liquid droplets.

The median profiles extracted from this cloud period reveal two distinct Ze_w profile characteristics (Fig. 5b). In the feeder part of the cloud, the measured Ze_w saturates likely from non-Rayleigh scattering by large ice particles with sizes comparable to the WProf wavelength. Indeed, the simulated size distribution of snow particles, supports the presence of large particles exceeding 1 mm at altitudes below 1 km above ground level (AGL) (Supplementary Fig. 5a). From the modeling perspective (Fig. 5c), at these altitudes, BR aligns with aggregation, but consistently generates an order of magnitude more particles per liter than aggregation depletes from snowflake number loss. The efficiency of BR maximizes closer to the surface, yielding almost $2 \bullet 10^{-2}$ small ice fragments per liter. Even though CONTROL and ALLSIP produce comparable snow number concentrations, yet the latter yields almost 2 orders of magnitude elevated cloud ice particle concentrations (Supplementary Fig. 8d). The subsequent growth of these particles via vapor deposition and riming (Fig. 5c) boosts the simulated Ze_w values leading to better agreement not only with the WProf reflectivity profile (Fig. 5b) but also with the LWP measurements during this period (Fig. 1f).

At higher altitudes and temperatures between approximately -16 and -25°C, WProf measured reduced Ze_w that is not reproduced by any WRF simulation (Fig. 5b). This discrepancy is likely from the presence of a dry layer separating the two clouds (Figs. 2a and Supplementary Fig. 6) that does not backscatter much signal to the radar. The timing and microphysics inside this cloud free region is likely more challenging to be captured by all model set-ups examined, but this does not appear to have a significant impact on ground precipitation and SIP. CONTROL generates cloud ice (Supplementary Fig. 8a) and snow particle (Supplementary Fig. 8b) concentrations one order of magnitude higher than DEMOTT at an altitude of ~2.2 km, which is nearly one (two) orders of magnitude elevated cloud ice (snow) concentrations compared to ALLSIP. The elevated concentrations of larger ice particles are probably causing the overestimated Ze_w values in CONTROL and DEMOTT. At these temperatures, initiation of BR in the ALLSIP simulation is found to shift the particle distributions towards smaller sizes, effectively moving the simulated Ze_w values closer to the observed IQR at the appropriate altitude and timing. Additionally, it is worth noting the contribution of SUBBR within the subsaturated air layer that separates the seeder from the feeder cloud regions, generating up to 10^{-5} particles per liter. This observation aligns with findings presented in Deshmukh [69] (see their Fig. 14).

When reviewing the skewness timeseries in Fig. 1e, we consistently notice positively skewed distributions, between mostly the -15°C and -20°C isotherms, persisting throughout the entire seeder-feeder cloud period. This reaffirms our earlier hypothesis regarding the connection between positive skewness, spectral bimodality, and processes such as BR and aggregation, as previously highlighted during the nimbostratus cloud period. Alltogether, this underscores once more the significance of incorporating SIP descriptions within the microphysics scheme of the WRF model, and the usefulness of the coupled model-radar simulator approach to reliably interpret the radar reflectivity signals.

DISCUSSION

Our WRF simulations highlight the crucial role of incorporating advanced SIP descriptions within the microphysics scheme of models to capture the underlying mechanisms affecting ice particle growth, multiplication, and consequent precipitation production. SIP significantly amplifies simulated cloud ice and snow concentrations by 1-2 orders of magnitude; BR-driven SIP initiates near the upper edge of the DGL (colder temperatures), with substantial snow and graupel particles colliding and generating small ice fragments. As these ice particles encounter warmer temperatures within mixed-phase conditions, they efficiently grow through vapor deposition and riming, fostering differential settling and enabling further aggregation-driven growth. This cascade effect ultimately contributes to increased snowfall near the ground, resulting in elevated reflectivities, that can be replicated solely through WRF simulations considering SIP. Rapid aggregation and vapor deposition of dendritic ice particles enhances differential settling, which increases collision probabilities and BR. The competition between BR and aggregation determines the modelled ICNCs. Upon entering low-level mixed-phase cloud regions, BR produces approximately tenfold more ice crystals than those depleted through aggregation.

Integration of modeling and remote sensing tools helps decipher microphysical signatures in observed full Doppler spectra. Using WRF with all SIP mechanisms active, we interpret observed spectral bimodalities for internal and external seeding cases. The faster-falling spectral mode was associated with the aggregate population, while distinct secondary modes emerged at temperatures around -18°C to -16°C coincided with enhanced BR and aggregation in WRF with remarkably good temporal and spatial alignment with an increase in the observed skewness timeseries. Persistent positive skewness arose within the DGL due to the spectra shift toward the slower-falling peak after SIP initiation. These findings propose strong connections between positive skewness, Doppler spectral bimodalities, aggregation, and SIP through BR within the DGL in the SIP temperature regime. Correct prediction of the vertical distribution of INPs is also key for getting the right balance of primary and secondary ice production, as well as the microphysical evolution of MPCs.

Overall, the presence of multi-modalities in the radar Doppler spectra, particularly within the DGL, has long underlined the need to improve our understanding of the intricate microphysical interactions taking place. Here we show that SIP, through BR, skews Doppler spectra towards the slower-falling side within the DGL. Confirming the existence of this radar signature in various cases worldwide opens the path for systematically deducing the occurrence of SIP through BR, even in remote Arctic [32] and Antarctic [70] regions, where long radar timeseries are abundant. The methodology proposed in this study offers unique insights that would otherwise be challenging to attain.

METHODS

CALISHTO campaign

The CALISHTO field campaign took place between October 2021 and March 2022 at Mount Helmos, Greece, with the primary objective of enhancing our understanding of the processes involved in orographic MPC formation and evolution. In this campaign, extensive in-situ and remote sensing

observations were carried out at three different altitudes. Meteorological, aerosol, and cloud measurements were taken at the mountain-top station, $(HAC)^2$, located at 2314 m AMSL (37°N 59' 2.4", 22°E 11' 45.6") (Supplementary Fig. 3) [58]. At the VL station, located on the lee side of $(HAC)^2$, aerosol and cloud measurements were conducted using remote sensing techniques. At the lower altitude site, ~1700 m AMSL, a multi-wavelength depolarization lidar was used to sample vertical profiles of aerosol and cloud properties.

Cloud in-situ measurements were conducted at $(HAC)^2$ using the Gerber Particulate Volume Monitor (PVM-100, Gerber Scientific Instruments Inc.) [71]. This instrument is designed to measure the LWC, particle surface area (PSA), and derive the droplet effective radius (r_{eff}) for ambient clouds. To obtain these measurements, a diode-emitted laser beam is directed along a 40-cm path, and the scattered light in the open air along the path is converted into a signal after passing two spatial filters. The first filter converts scattered light to a signal proportional to the particle volume density (or LWC), while the second filter produces a signal proportional to the PSA. By analyzing the ratio of these two quantities, r_{eff} can be derived for droplet diameter from 3 to 45 μm. The uncertainty of LWC is 10 % for this diameter range. The PVM-100 instrument has undergone testing and inter-comparison with other instruments during ACTRIS (Aerosol Cloud and Trace gases Research Infrastructure) activities [72]. For the purposes of this study, LWC and r_{eff} data collected by the PVM-100 were utilized to derive the cloud droplet number concentration (N_d) based on the formulation presented in Brazda et al. (2013) (see their Equation 4).

Aerosol size distributions over the size range between 0.25 and 32 μm were measured at $(HAC)^2$ by an Optical Particle Counter (OPC; GRIMM Technologies Inc., Model 1.109), which provides real-time aerosol characterization including 32 channels. In this study, OPC diameter (d_{opc}) was converted into aerodynamic diameter (d_{aer}) using the formula: , assuming a shape factor of χ=1.1 and a particle density of ρ=2.0 g cm^{-3} [74,75].

Remote sensing observations

At the VL station, a frequency-modulated continuous wave (FMCW) W-band Doppler spectral zenith profiler (WProf) [57] was deployed. Operating at a frequency of 94 GHz, WProf allows for measurements up to approximately 10 km above gound level. Vertically, WProf employs three chirps, each with a respective range resolution of 7.5 m, 16 m, and 32 m. WProf settings are summarized in the Supplementary Table 1. For this study, we utilized full Doppler reflectivity spectra and corresponding moments. These moments include the Ze_w, MDV and skewness. An attenuation correction has been applied to the W-band radar reflectivities, to facilitate their comparison against the forward simulation products. To do so, the radiative transfer model PAMTRA [76] was used to simulate both gaseous and cloud liquid water attenuation at 94 GHz. The vertical profiles of the necessary atmospheric and liquid water profiles were obtained from the WRF model set-up, which includes the most advanced description of both primary and secondary sources of ice crystals (see ALLSIP simulation described below).

In addition to the radar variables, WProf offers the capability to estimate the cloud LWP using a retrieval algorithm presented by Billault-Roux and Berne [77]. This algorithm uses the brightness temperature measured by a joint 89-GHz radiometer, in combination with available meteorological data such as temperature, pressure, and reanalysis data as well as geographical information (i.e., latitude, longitude). The relative error in the retrieved LWP values was determined to be 18% for cloudy cases (i.e., LWP > 30 g m^{-2}).

WRF model set-up

We utilized WRF version 4.0.1, incorporating augmented cloud microphysics to account for additional SIP mechanisms [35,62,78], to model the current case study. Our model configuration consisted of three two-way nested domains (Supplementary Fig. 3a) with horizontal resolutions of 12 km, 3 km, and 1 km, respectively. The parent domain encompassed a 148x148 grid centered over the $(HAC)^2$ station. The second and third domains consisted of 241x241 and 304x304 grids, respectively. All domains employed the Lambert conformal projection, suitable for mid-latitudes. We implemented a refined vertical grid spacing, following the approach proposed by Vignon [55], employing 97 vertical eta levels up to a model top of 50 hPa (~20 km). Note that the employed model setup was consistent with the one utilized for wintertime orographic clouds in the Swiss Alps [62].

The WRF simulations started on December 17, 2021, at 00:00 UTC, providing 22 hours of spin-up time before the passage of storm Carmel over the region of interest. This low-pressure system was associated with polar airmasses originating from northern Europe (Supplementary Fig. 9), bringing a significant temperature decrease, stormy winds, and heavy snowfall to most parts of Central and Southern Greece. The temperature drop and the prevailing strong-wind conditions are illustrated in Supplementary Fig. 2, where they are compared against surface meteorological variables obtained from the weather station at $(HAC)^2$ to evaluate the performance of the model. Our analysis covers the period until December 19, 2021, at 12:00 UTC. We employed a time step of 36 s in the parent domain, which decreased to 9 s in the second domain and 3 s in the third domain. The output frequency was set at every 5 minutes. Information about the physics options employed here are provided in Supplementary Text 3.

Microphysics scheme and sensitivity simulations

Cloud microphysics is parameterized using the Morrison [79] (M05) scheme of WRF. This scheme utilizes a double-moment approach to represent the characteristics of raindrops, cloud ice, snow, and graupel particles by predicting both their mass and number concentrations. However, for cloud droplets, a single-moment approach is employed, necessitating the specification of a constant N_d. During the passage of storm Carmel, a power outage caused by severe weather conditions disrupted the PVM-100 measurements. In our study, we opted for an N_d value of 100 cm^{-3}. This choice aligns with the temperature-dependent median N_d spectrum observed by PVM-100 throughout the CALISHTO campaign and is also consistent with observations at the high-altitude station of Jungfraujoch in the Swiss Alps [80].

The M05 scheme incorporates different ice formation processes. Homogeneous freezing is considered for temperatures below -40°C, while heterogeneous ice nucleation is initiated below -4°C. The latter accounts for various temperature-dependent mechanisms, including immersion freezing of cloud droplets and raindrops [81], contact freezing [82], and condensation/deposition freezing nucleation [83]. The default PIP scheme of WRF was used to perform the CONTROL sensitivity simulation. However, when comparing the predicted INPs derived offline using the simplified temperature-dependent formulations of WRF with two-month INP measurements taken between -28°C and -23°C at $(HAC)^2$, a significant overestimation of up to three orders of magnitude was observed (Supplementary Fig. 10b, c, Supplementary Text 4). As a more advanced alternative, DeMott [60] (DM10) developed an aerosol-aware scheme that accounts for the concentration of aerosols with sizes larger than 0.5 µm aerodynamic diameter ($n_{aer,0.5}$) and temperature. The DM10 parameterization yielded more realistic offline INP concentrations, with predictions that agree with observations within a factor of three (Supplementary Fig. 10a) for more than 70% observed data points. Therefore, in the DEMOTT sensitivity simulation, we replaced the default PIP scheme of WRF with the DM10 parameterization. In our case an $n_{aer,0.5}$ of 0.30 scm^{-3} was prescribed, as dictated by the mean OPC measurements taken during the simulation period. Note that in DEMOTT, the Bigg [81] parameterization was still kept active to account for the freezing of big raindrops.

The final sensitivity simulation analyzed in this study, referred to as ALLSIP, incorporates both PIP and SIP processes, with the former following the advanced DM10 parameterization. The M05 scheme, similar to other microphysics schemes in NWP models, includes the representation of only one SIP process: HM. This process is parameterized following Reisner [84], which accounts for the production of ice splinters within the HM temperature range ($-8 \leq T \leq -3$°C). It occurs when supercooled droplets or raindrops collide and freeze onto snow or graupel particles. Provided that a certain threshold in the mixing ratios of the involved ice and liquid hydrometeors is exceeded, the efficiency of this process is regulated by a temperature-dependent scaling factor which allows for a maximum production rate of 350 splinters per milligram of accreted liquid, at around -5°C [84]. The splinter production rate decreases linearly towards the edges of the HM zone and becomes zero outside this range.

The BR mechanism is an additional SIP process considered in ALLSIP. In the M05 scheme, BR follows the parameterization by Phillips [40], which has been shown to provide realistic representation of ICNCs in orographic MPCs [62]. A detailed implementation of the BR mechanism in M05 is described in [35]. The number of ice fragments generated from collisions among the three ice hydrometeor species is determined by factors such as collisional kinetic energy, size, rimed fraction, and ice habit of the particles involved. While M05 does not explicitly resolve the rimed fraction and ice habit, assumptions are made to account for their influence. The impact of the prescribed rimed fraction has been previously investigated [35,85], and a sensitivity experiment in the current case study revealed that a rimed fraction of 0.2 aligns better with observed cloud systems (not shown). Higher degrees of riming led to unrealistically high ICNCs, particularly within the lower cloud layers. Activation of BR requires a nonzero mass of raindrop or cloud droplet to be rimed onto the ice particle, leading to fragmentation. It is important to note

that the original BR scheme was designed for ice particles larger than 500 μm. According to Phillips [40], when dealing with smaller sizes, it is advisable to set them to the nearest limit within the specified range. Consequently, we limit the efficiency of BR to particles with a characteristic size exceeding 100 μm. Regarding the ice habit, the Phillips parameterization provides two formulations depending on the prevailing temperature range. Dendritic particles are considered between -17 and -12°C, while non-dendritic planar ice particles are assumed outside this temperature range. Sotiropoulou [85] found minimal sensitivity to the prescribed ice habit, and thus we adopt planar ice particles, which capture a wider temperature range and are valid for a broader range of particle shapes. All secondary ice fragments resulting from the BR mechanism are classified as cloud ice.

Another SIP process accounted for in ALLSIP is the DS mechanism. A detailed description of how M05 scheme was updated to include this process is provided in Georgakaki [62]. DS involves two collision modes, as outlined by Phillips [86]. In the first mode, freezing and subsequent shattering occur when a supercooled raindrop collides with a less massive cloud ice particle or when an INP triggers freezing in immersion mode. The number of fragments generated in this mode are multiplied by the product of droplet freezing and shattering probabilities, being described by the cubic interpolation functions found in Phillips [86]. The former is set to unity for temperatures below -6°C and zero for temperatures above -3°C, while the latter depends on the size of the raindrop, being 0 for sizes smaller than 50 μm, 1 for sizes larger than 60 μm. The second mode, involves collisions between raindrops and larger ice particles such as snow or graupel [25]. These collisions produce tiny ice fragments, which are introduced as cloud ice in the number conservation equations. Larger fragments are classified depending on the specific collision that triggered the freezing process of raindrops, which will in turn determine whether they will be treated as graupel, snow, or frozen drops.

The last SIP process included in ALLSIP is SUBBR, which occurs when dendritic or heavily rimed particles sublimate under subsaturated conditions within downdrafts, resulting in the detachment of ice parts (e.g., branches from dendrites) from the parent ice particle [47]. A recent study by Deshmukh [69] introduced two empirical formulations for the SUBBR of graupel and dendritic snow. When implemented into the M05 scheme, the former parameterization is valid throughout all temperatures provided that the RH_i is less than 100%. The latter is enabled at temperatures between $-20 \leq T \leq -10$ °C, where the dendritic ice habit of snow particles is favored [87]. The number of fragments generated after SUBBR ( ) is determined by the product: , where K is a function of the initial size of the particle, ambient RH_i, and a ventilation factor associated with the fall speed of the particle, while M is the sublimated mass described by the M05 scheme. More details about this empirical parameterization can be found in Deshmukh [69].

The CR-SIM forward radar simulator

Forward simulators are valuable tools for converting model output into quantities that can be directly compared with observations from remote sensing instruments. This enables a more accurate assessment of the agreement between model predictions and real-world data. In our study, we utilized the

outputs from the 3 WRF sensitivity simulations (i.e., CONTROL, DEMOTT, and ALLSIP) as input for the Cloud Resolving Model Radar Simulator (CR-SIM) version 3.32 [54]. CR-SIM is compatible with various microphysics schemes of WRF and has previously been employed to evaluate the performance of polar WRF in representing Southern Ocean MPCs and snowfall microphysics [55,56]. The T-matrix method is used in CR-SIM to calculate the scattering properties of simulated frozen and liquid hydrometeors, which are then organized into look-up tables. In our study, CR-SIM was configured as a vertically profiling radar operating at 94 GHz, matching the frequency of the WProf deployed at VL. The radar beamwidth and range resolution were also adjusted to align with the characteristics of the actual instrument. The CR-SIM was run using a specific model grid point located closer to the VL station. The idealized simulated radar variables (i.e., after correction for the total hydrometeor attenuation) are then provided at each vertical model grid cell, facilitating straightforward comparisons with real observations.

Declarations

DATA AVAILABILITY

The WRF outputs from the three sensitivity simulations as well as the remote sensing observations will be made available at https://www.envidat.ch.

CODE AVAILABILITY

The original WRF code used in this study (version 4.0.1) is open source and can be accessed at (https://github.com/wrf-model/WRF). The updated microphysics scheme is available upon request from the corresponding authors.

ACKNOWLEDGEMENTS

Funding for this study was provided by the European Research Council (ERC) project “PyroTRACH” (Grant agreement No. 726165) and the European Union’s Horizon 2020 project “FORCeS” (Grant agreement No. 821205). Further funding was provided in the frame of the PANhellenic infrastructure for Atmospheric Composition and climatE change (PANACEA) research project (MIS 5021516), implemented under the Action Reinforcement of the Research and Innovation Infrastructure, and the Operational Program Competitiveness, Entrepreneurship, and Innovation (NSRF 2014–2020), co-financed by Greece and the European Union (European Regional Development Fund). RF was also supported by the Basic Research Program, NTUA (PEVE) under contract PEVE0011/2021.

AUTHOR CONTRIBUTIONS

AN and PG conceived and lead the study. PG conducted the WRF simulations, set up the radar simulator and analysed the results. AN, AP and KE lead and coordinated the CALISHTO campaign. The radar instrumentation was setup and run by RF throughout the CALISHTO camapaign. ACBR performed post-processing on the radar observations and, along with AB interpreted the data. MG, KE also provided data

from the $(HAC)^2$ station, while KG analyzed the primary ice nuclei data presented in Supplementary Fig. 10a. GS contributed to the implementation of the sublimational break-up mechanism parameterization, while ST helped with statistical interpretation of the radar simulator output. PG together with AN worked on the manuscript, and all co-authors provided feedback.

COMPETING INTERESTS

The authors declare no competing interests.

References

1. Vergara-Temprado, J. *et al.* Strong control of Southern Ocean cloud reflectivity by ice-nucleating particles. *Proc. Natl. Acad. Sci. U. S. A.* **115**, 2687–2692 (2018).
2. Tan, I. & Storelvmo, T. Evidence of Strong Contributions From Mixed-Phase Clouds to Arctic Climate Change. *Geophys. Res. Lett.* **46**, 2894–2902 (2019).
3. Heymsfield, A. J. *et al.* Contributions of the Liquid and Ice Phases to Global Surface Precipitation: Observations and Global Climate Modeling. *J. Atmos. Sci.* **77**, 2629–2648 (2020).
4. Mülmenstädt, J., Sourdeval, O., Delanoë, J. & Quaas, J. Frequency of occurrence of rain from liquid-, mixed-, and ice-phase clouds derived from A-Train satellite retrievals. *Geophys. Res. Lett.* **42**, 6502–6509 (2015).
5. Korolev, A. V., Isaac, G. A., Cober, S. G., Strapp, J. W. & Hallett, J. Microphysical characterization of mixed-phase clouds. *Q. J. R. Meteorol. Soc.* **129**, 39–65 (2003).
6. Field, P. R. *et al.* Simultaneous radar and aircraft observations of mixed-phase cloud at the 100 m scale. *Q. J. R. Meteorol. Soc.* **130**, 1877–1904 (2004).
7. Korolev, A. & Milbrandt, J. How Are Mixed-Phase Clouds Mixed? *Geophys. Res. Lett.* **49**, (2022).
8. Bergeron, T. On the physics of clouds and precipitation. *Report, Int. Union Geod. Geophys.* (1935) doi:10.1038/174957a0.
9. Findeisen, W. Die kolloidmeteorologischen vorgänge bei der niederschlagsbildung. *Meteorol. Zeitschrift* **55**, 121–133 (1938).
10. Wegener, A. Thermodynamik der Atmosphäre. *Ger. Barth,Leipzig* 331 pp. (1911).
11. Matus, A. V. & L'Ecuyer, T. S. The role of cloud phase in Earth's radiation budget. *J. Geophys. Res.* **122**, 2559–2578 (2017).
12. McCoy, D. T., Tan, I., Hartmann, D. L., Zelinka, M. D. & Storelvmo, T. On the relationships among cloud cover, mixed-phase partitioning, and planetary albedo in GCMs. *J. Adv. Model. Earth Syst.* **8**, 650–668 (2016).
13. Zelinka, M. D. *et al.* Causes of Higher Climate Sensitivity in CMIP6 Models. *Geophys. Res. Lett.* **47**, 1–12 (2020).
14. Hoose, C. & Möhler, O. *Heterogeneous ice nucleation on atmospheric aerosols: A review of results from laboratory experiments*. *Atmospheric Chemistry and Physics* vol. 12 (2012).

15. Murray, B. J., O'Sullivan, D., Atkinson, J. D. & Webb, M. E. Ice nucleation by particles immersed in supercooled cloud droplets. *Chem. Soc. Rev.,* **41**, 6519–6554 (2012).
16. Kanji, Z. A. *et al.* Overview of Ice Nucleating Particles. *Meteorol. Monogr.* **58**, 1.1-1.33 (2017).
17. Wex, H. *et al.* Annual variability of ice-nucleating particle concentrations at different Arctic locations. *Atmos. Chem. Phys.* **19**, 5293–5311 (2019).
18. Field, P. R. *et al.* Chapter 7. Secondary Ice Production - current state of the science and recommendations for the future. *Meteorol. Monogr.* **58**, (2017).
19. Korolev, A. & Leisner, T. *Review of experimental studies of secondary ice production*. *Atmospheric Chemistry and Physics* vol. 20 (2020).
20. Huang, Y. *et al.* Microphysical processes producing high ice water contents (HIWCs) in tropical convective clouds during the HAIC-HIWC field campaign: Dominant role of secondary ice production. *Atmos. Chem. Phys.* **22**, 2365–2384 (2022).
21. Young, G. *et al.* Radiative Effects of Secondary Ice Enhancement in Coastal Antarctic Clouds. *Geophys. Res. Lett.* **46**, 2312–2321 (2019).
22. Zhao, X. *et al.* Important Ice Processes Are Missed by the Community Earth System Model in Southern Ocean Mixed-Phase Clouds: Bridging SOCRATES Observations to Model Developments. *J. Geophys. Res. Atmos.* **128**, 1–15 (2023).
23. Grzegorczyk, P. *et al.* Fragmentation of ice particles : laboratory experiments on graupel-graupel and graupel-snowflake collisions. *Atmos. Chem. Phys. Discuss.* (2023) doi:10.5194/egusphere-2023-1074.
24. Keinert, A., Spannagel, D., Leisner, T. & Kiselev, A. Secondary ice production upon freezing of freely falling drizzle droplets. *J. Atmos. Sci.* **77**, 2959–2967 (2020).
25. James, R. L., Phillips, V. T. J. & Connolly, P. J. Secondary ice production during the break-up of freezing water drops on impact with ice particles. *Atmos. Chem. Phys. Discuss.* **21**, 18519–18530 (2021).
26. Vardiman, L. The generation of secondary ice particles in clouds by crystal-crystal collision. *J. Atmos. Sci.* **35**, 2168–2180 (1978).
27. Lasher-Trapp, S. *et al.* A multisensor investigation of rime splintering in tropical maritime cumuli. *J. Atmos. Sci.* **73**, 2547–2564 (2016).
28. Lawson, R. P., Woods, S. & Morrison, H. The microphysics of ice and precipitation development in tropical cumulus clouds. *J. Atmos. Sci.* **72**, 2429–2445 (2015).
29. Järvinen, E. *et al.* Evidence for Secondary Ice Production in Southern Ocean Maritime Boundary Layer Clouds. *J. Geophys. Res. Atmos.* **127**, 1–31 (2022).
30. Billault-Roux, A.-C. *et al.* Distinct secondary ice production processes observed in radar Doppler spectra : insights from a case study. *Atmos. Chem. Phys. Discuss.* (2023) doi:10.5194/egusphere-2023-478.

31. Grazioli, J. *et al.* Polarimetric radar and in situ observations of riming and snowfall microphysics during CLACE 2014. *Atmos. Chem. Phys.* **15**, 13787–13802 (2015).
32. Luke, E. P., Yang, F., Kollias, P., Vogelmann, A. M. & Maahn, M. New insights into ice multiplication using remote-sensing observations of slightly supercooled mixed-phase clouds in the Arctic. *Proc. Natl. Acad. Sci. U. S. A.* **118**, 1–9 (2021).
33. Li, H., Möhler, O., Petäjä, T. & Moisseev, D. Two-year statistics of columnar-ice production in stratiform clouds over Hyytiälä, Finland: Environmental conditions and the relevance to secondary ice production. *Atmos. Chem. Phys.* **21**, 14671–14686 (2021).
34. Atlas, R. L. *et al.* How Well Do Large-Eddy Simulations and Global Climate Models Represent Observed Boundary Layer Structures and Low Clouds Over the Summertime Southern Ocean? *J. Adv. Model. Earth Syst.* **12**, 1–25 (2020).
35. Sotiropoulou, G. *et al.* Secondary ice production in summer clouds over the Antarctic coast: An underappreciated process in atmospheric models. *Atmos. Chem. Phys.* **21**, 755–771 (2021).
36. Zhao, X. & Liu, X. Global Importance of Secondary Ice Production. *Geophys. Res. Lett.* **48**, 1–11 (2021).
37. Hoose, C. Another Piece of Evidence for Important but Uncertain Ice Multiplication Processes. *AGU Adv.* **3**, 2021–2023 (2022).
38. Hallett, J. & Mossop, S. C. Production of secondary ice particles during the riming process. *Nature* **249**, 26–28 (1974).
39. Heymsfield, A. J. & Mossop, S. C. Temperature dependence of secondary ice crystal production during soft hail growth by riming. *Q. J. R. Meteorol. Soc.* **110**, 765–770 (1984).
40. Phillips, V. T. J., Yano, J. I. & Khain, A. Ice multiplication by breakup in ice-ice collisions. Part I: Theoretical formulation. *J. Atmos. Sci.* **74**, 1705–1719 (2017).
41. Takahashi, T., Nagao, Y. & Kushiyama, Y. Possible high ice particle production during graupel-graupel collisions. *J. Atmos. Sci.* **52**, 4523–4527 (1995).
42. Griggs, D. J. & Choularton, T. W. Freezing modes of riming droplets with application to ice splinter production. *Q. J. R. Meteorol. Soc.* **109**, 243–253 (1983).
43. Lauber, A., Kiselev, A., Pander, T., Handmann, P. & Leisner, T. Secondary ice formation during freezing of levitated droplets. *J. Atmos. Sci.* **75**, 2815–2826 (2018).
44. Hartmann, S. *et al.* Secondary ice production - No evidence of a productive rime-splintering mechanisms during dry and wet growth. in *EGU General Assembly 2023, Vienna, Austria* (2023). doi:https://doi.org/10.5194/egusphere-egu23-11199.
45. Patade, S. *et al.* The influence of multiple groups of biological ice nucleating particles on microphysical properties of mixed-phase clouds observed during MC3E. *Atmos. Chem. Phys.* **22**, 12055–12075 (2022).
46. Waman, D. *et al.* Dependencies of Four Mechanisms of Secondary Ice Production on Cloud-Top Temperature in a Continental Convective Storm. *J. Atmos. Sci.* **79**, 3375–3404 (2022).

47. Bacon, N. J., Swanson, B. D., Baker, M. B. & Davis, E. J. Breakup of levitated frost particles. *J. Geophys. Res. Atmos.* **103**, 13763–13775 (1998).
48. Li, H., Korolev, A. & Moisseev, D. Supercooled liquid water and secondary ice production in Kelvin-Helmholtz instability as revealed by radar Doppler spectra observations. *Atmos. Chem. Phys.* **21**, 13593–13608 (2021).
49. Oue, M., Kollias, P., Ryzhkov, A. & Luke, E. P. Toward Exploring the Synergy Between Cloud Radar Polarimetry and Doppler Spectral Analysis in Deep Cold Precipitating Systems in the Arctic. *J. Geophys. Res. Atmos.* **123**, 2797–2815 (2018).
50. Wieder, J. *et al.* Retrieving ice-nucleating particle concentration and ice multiplication factors using active remote sensing validated by in situ observations. *Atmos. Chem. Phys.* **22**, 9767–9797 (2022).
51. von Terzi, L., Dias Neto, J., Ori, D., Myagkov, A. & Kneifel, S. Ice microphysical processes in the dendritic growth layer: a statistical analysis combining multi-frequency and polarimetric Doppler cloud radar observations. *Atmos. Chem. Phys.* **22**, 11795–11821 (2022).
52. Kalesse, H., Szyrmer, W., Kneifel, S., Kollias, P. & Luke, E. Fingerprints of a riming event on cloud radar Doppler spectra: Observations and modeling. *Atmos. Chem. Phys.* **16**, 2997–3012 (2016).
53. Oue, M. *et al.* Linear depolarization ratios of columnar ice crystals in a deep precipitating system over the arctic observed by zenith-pointing Ka-band doppler radar. *J. Appl. Meteorol. Climatol.* **54**, 1060–1068 (2015).
54. Oue, M. *et al.* The Cloud-resolving model Radar SIMulator (CR-SIM) Version 3.3: Description and applications of a virtual observatory. *Geosci. Model Dev.* **13**, 1975–1998 (2020).
55. Vignon, É. *et al.* Challenging and Improving the Simulation of Mid-Level Mixed-Phase Clouds Over the High-Latitude Southern Ocean. *J. Geophys. Res. Atmos.* **126**, 1–21 (2021).
56. Vignon, Besic, N., Jullien, N., Gehring, J. & Berne, A. Microphysics of Snowfall Over Coastal East Antarctica Simulated by Polar WRF and Observed by Radar. *J. Geophys. Res. Atmos.* **124**, 11452–11476 (2019).
57. Küchler, N. *et al.* A W-band radar-radiometer system for accurate and continuous monitoring of clouds and precipitation. *J. Atmos. Ocean. Technol.* **34**, 2375–2392 (2017).
58. Coen, M. C. *et al.* Identification of topographic features influencing aerosol observations at high altitude stations. *Atmos. Chem. Phys.* **18**, 12289–12313 (2018).
59. Proske, U., Bessenbacher, V., Dedekind, Z., Lohmann, U. & Neubauer, D. How frequent is natural cloud seeding from ice cloud layers (<-35°C) over Switzerland? *Atmos. Chem. Phys.* **21**, 5195–5216 (2021).
60. DeMott, P. J. *et al.* Predicting global atmospheric ice nuclei distributions and their impacts on climate. *Proc. Natl. Acad. Sci.* **107**, 11217–11222 (2010).
61. Thomas, J., Barrett, A. & Hoose, C. Temperature and cloud condensation nuclei (CCN) sensitivity of orographic precipitation enhanced by a mixed-phase seeder-feeder mechanism: a case study for the 2015 Cumbria flood. *Atmos. Chem. Phys.* **23**, 1987–2002 (2023).

62. Georgakaki, P. *et al.* Secondary ice production processes in wintertime alpine mixed-phase clouds. *Atmos. Chem. Phys.* **22**, 1965–1988 (2022).
63. Phillips, V. T. J. *et al.* Ice multiplication by breakup in ice-ice collisions. Part II: Numerical simulations. *J. Atmos. Sci.* **74**, 2789–2811 (2017).
64. Dedekind, Z., Grazioli, J., Austin, P. H. & Lohmann, U. Heavy snowfall event over the Swiss Alps: did wind shear impact secondary ice production? *Atmos. Chem. Phys.* **23**, 2345–2364 (2023).
65. Yang, J., Lei, H., Hu, Z. & Hou, T. Particle size spectra and possible mechanisms of high ice concentration in nimbostratus over hebei province, china. *Atmos. Res.* **142**, 79–90 (2014).
66. Kneifel, S. & Moisseev, D. Long-term statistics of riming in nonconvective clouds derived from ground-based doppler cloud radar observations. *J. Atmos. Sci.* **77**, 3495–3508 (2020).
67. Orr, B. W. & Kropfli, R. A. A method for estimating particle fall velocities from vertically pointing Doppler radar. *J. Atmos. Ocean. Technol.* **16**, 29–37 (1999).
68. Giangrande, S. E. *et al.* Insights into riming and aggregation processes as revealed by aircraft, radar, and disdrometer observations for a 27 April 2011 widespread precipitation event. *J. Geophys. Res. Atmos.* **121**, 5846–5863 (2016).
69. Deshmukh, A., Phillips, V. T. J., Bansemer, A., Patade, S. & Waman, D. New Empirical Formulation for the Sublimational Breakup of Graupel and Dendritic Snow. *J. Atmos. Sci.* **79**, 317–336 (2022).
70. Ferrone, A. & Berne, A. Radar and ground-level measurements of clouds and precipitation collected during the POPE 2020 campaign at Princess Elisabeth Antarctica. *Earth Syst. Sci. Data* **15**, 1115–1132 (2023).
71. Gerber, H. Direct measurement of suspended particulate volume concentration and far-infrared extinction coefficient with a laser diffraction instrument. *Appl. Opt.* **30**, 4824–4831 (1991).
72. Guyot, G. *et al.* Quantitative evaluation of seven optical sensors for cloud microphysical measurements at the Puy-de-Dôme Observatory, France. *Atmos. Meas. Tech.* **8**, 4347–4367 (2015).
73. Brazda, V. *et al.* Cloud microphysics from the free space optical link point of view - Preliminary experimental results. *Proc. 2013 2nd Int. Work. Opt. Wirel. Commun. IWOW 2013* 63–66 (2013) doi:10.1109/IWOW.2013.6777778.
74. Hu, M. *et al.* Estimation of size-resolved ambient particle density based on the measurement of aerosol number, mass, and chemical size distributions in the winter in Beijing. *Environ. Sci. Technol.* **46**, 9941–9947 (2012).
75. Peters, T. M., Ott, D. & O'Shaughnessy, P. T. Comparison of the Grimm 1.108 and 1.109 portable aerosol spectrometer to the TSI 3321 aerodynamic particle sizer for dry particles. *Ann. Occup. Hyg.* **50**, 843–850 (2006).
76. Mech, M. *et al.* PAMTRA 1.0: The Passive and Active Microwave radiative TRAnsfer tool for simulating radiometer and radar measurements of the cloudy atmosphere. *Geosci. Model Dev.* **13**, 4229–4251 (2020).

77. Billault-Roux, A.-C. & Berne, A. Integrated water vapor and liquid water path retrieval using a single-channel radiometer. *Atmos. Meas. Tech.* **14**, 2749–2769 (2021).
78. Karalis, M. *et al.* Effects of secondary ice processes on a stratocumulus to cumulus transition during a cold-air outbreak. *Atmos. Res.* **277**, (2022).
79. Morrison, H., Curry, J. A., Shupe, M. D. & Zuidema, P. A new double-moment microphysics scheme for application in cloud and climate models. Part II: Single-column modeling of Arctic clouds. *J. Atmos. Sci.* **62**, 1678–1693 (2005).
80. Lloyd, G. *et al.* The origins of ice crystals measured in mixed-phase clouds at the high-alpine site Jungfraujoch. *Atmos. Chem. Phys.* **15**, 12953–12969 (2015).
81. Bigg, E. K. The formation of atmospheric ice crystals by the freezing of droplets. *Q. J. R. Meteorol. Soc.* **79**, 510–519 (1953).
82. Meyers, M. P., DeMott, P. J. & Cotton, W. R. New Primary Ice-Nucleation Parameterizations in an Explicit Cloud Model. *J. Appl. Meteorol.* **31**, 708–721 (1992).
83. Cooper, W. A. Ice Initiation in Natural Clouds. *Meteorol. Monogr.* **21**, 29–32 (1986).
84. Reisner, J., Rasmussen, R. M. & Bruintjes, R. T. Explicit forecasting of supercooled liquid water in winter storms using the MM5 mesoscale model. *Q. J. R. Meteorol. Soc.* **124**, 1071–1107 (1998).
85. Sotiropoulou, G., Ickes, L., Nenes, A. & Ekman, A. Ice multiplication from ice–ice collisions in the high Arctic: sensitivity to ice habit, rimed fraction, ice type and uncertainties in the numerical description of the process. *Atmos. Chem. Phys.* **21**, 9741–9760 (2021).
86. Phillips, V. T. J., Patade, S., Gutierrez, J. & Bansemer, A. Secondary ice production by fragmentation of freezing drops: Formulation and theory. *J. Atmos. Sci.* **75**, 3031–3070 (2018).
87. Libbrecht, K. G. Physical Dynamics of Ice Crystal Growth. *Annu. Rev. Mater. Res.* **47**, 271–295 (2017).

Figures

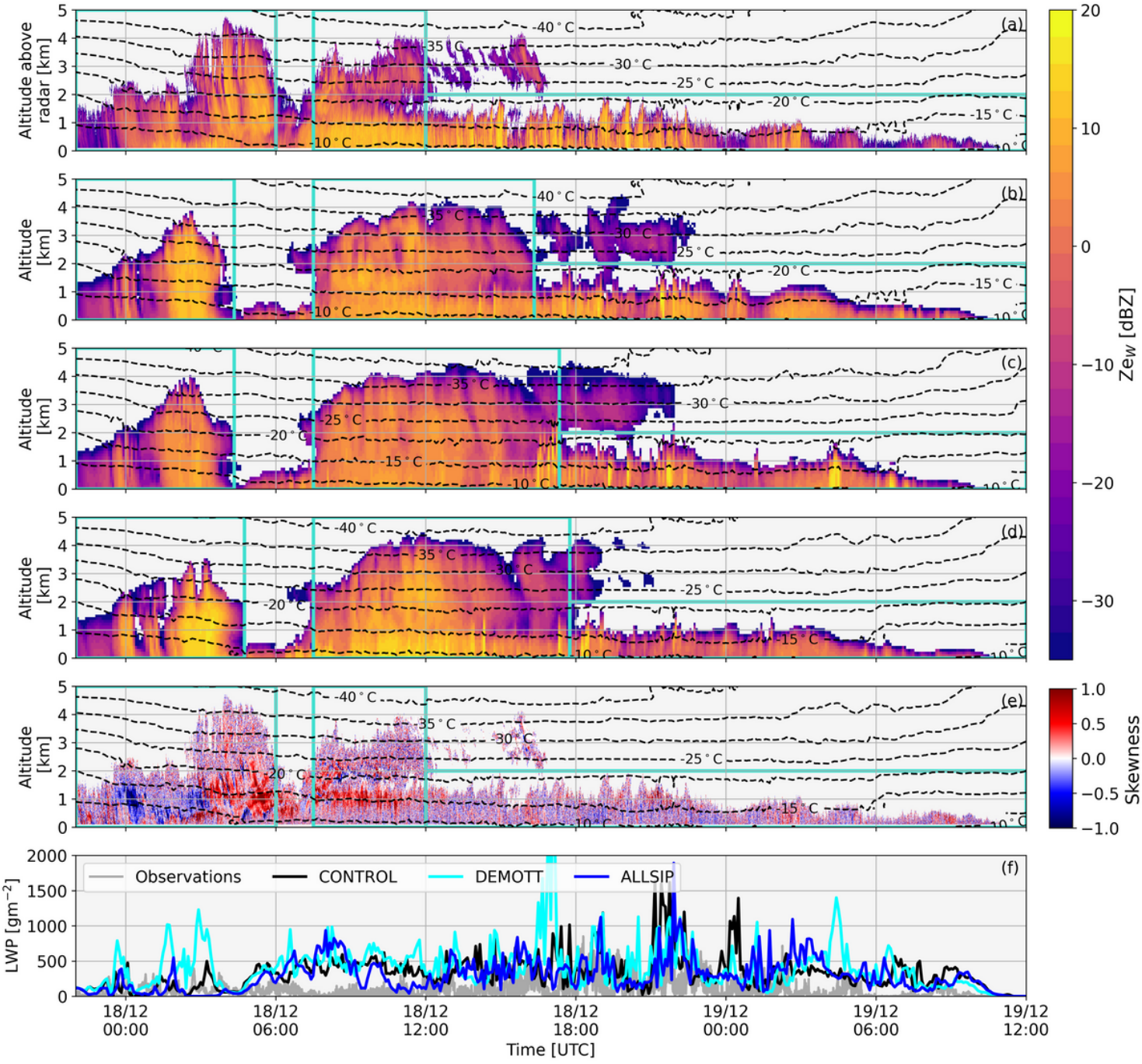

Figure 1

Time-height plots of radar reflectivity Ze_W from December 17 (22:00 UTC) to December 19 (12:00 UTC), 2021, displaying (a) measurements by the WProf radar deployed at VL, and simulations coupling the CR-SIM radar simulator with the (b) CONTROL, (c) DEMOTT, and (d) ALLSIP WRF model set-ups. The observed Doppler spectral skewness is also superimposed in panel (e). The LWP timeseries at VL, measured by the joint radiometer and simulated by WRF, is shown in the last panel (f). Note that the simulated LWP takes into account both cloud droplets and raindrops. The turquoise boxes indicate the three distinct cloud periods used to extract statistics. Temperature contours (in °C) are from the

CONTROL simulation of WRF in (a, b, e), and from the DEMOTT and ALLSIP simulations in (c) and (d), respectively.

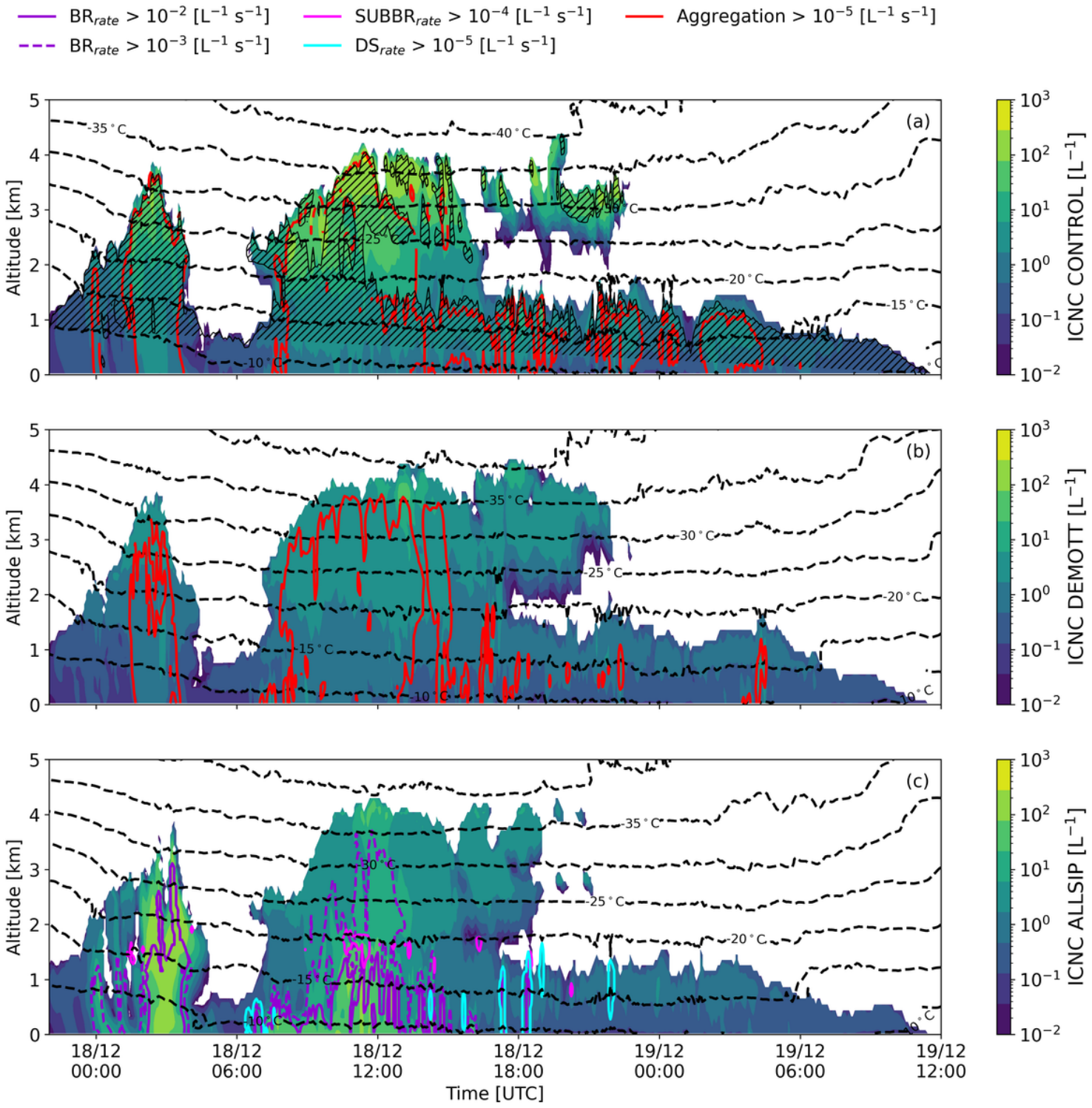

Figure 2

Time-height plots of total ICNCs produced by the (a) CONTROL, (b) DEMOTT, and (c) ALLSIP simulations for the period December 17 (22:00 UTC) to December 19 (12:00 UTC), 2021. The black contours in all panels represent temperature isotherms, while the red contours in (a) and (b) show areas where

snowflake aggregation rates exceed 10^{-5} $L^{-1}s^{-1}$. Note that the tendencies due to snow aggregation are presented in absolute values. The black hatched lines in (a) indicate regions that are supersaturated with respect to ice. In panel (c), the contours represent each active SIP rate: purple solid (dashed) contours indicate regions where BR rates exceed 10^{-2} (10^{-3}) L^{-1} s^{-1}, while cyan (magenta) contours show regions where DS (SUBBR) rates exceed 10^{-5} (10^{-4}) $L^{-1}s^{-1}$. Note that the tendencies of snowflake aggregation predicted by ALLSIP are presented in Supplementary Fig. 6.

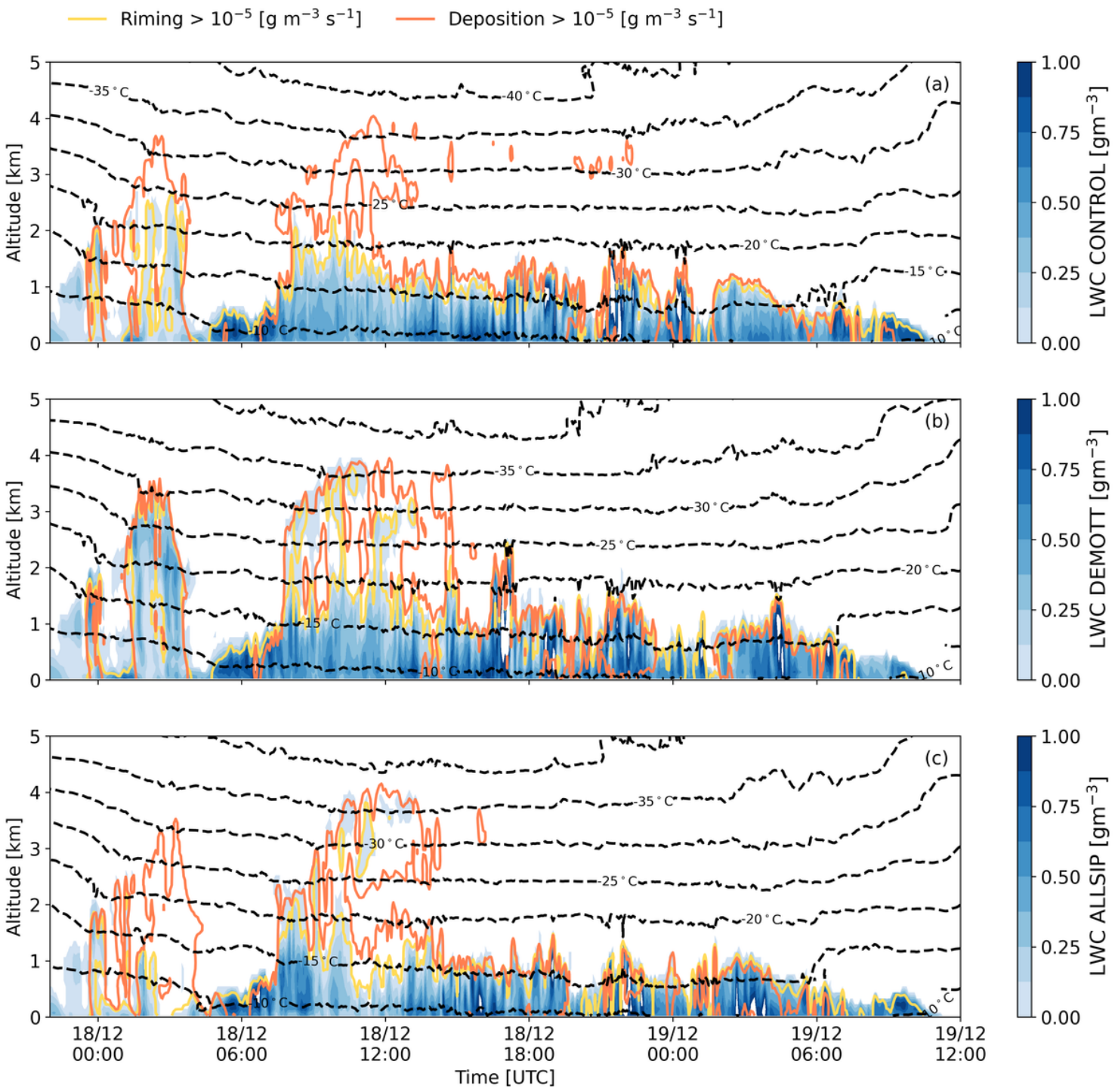

Figure 3

Same as in Fig. 2, but now the color shading represents the total LWC predicted by (a) CONTROL, (b) DEMOTT, and (c) ALLSIP simulations for the period December 17 (22:00 UTC) to December 19 (12:00 UTC), 2021. The black contour lines represent again the temperature isotherms, while in all three panels the yellow (orange) contours indicate the regions, where riming (vapor deposition) rates exceeds 10^{-5} g m^{-3} s^{-1}.

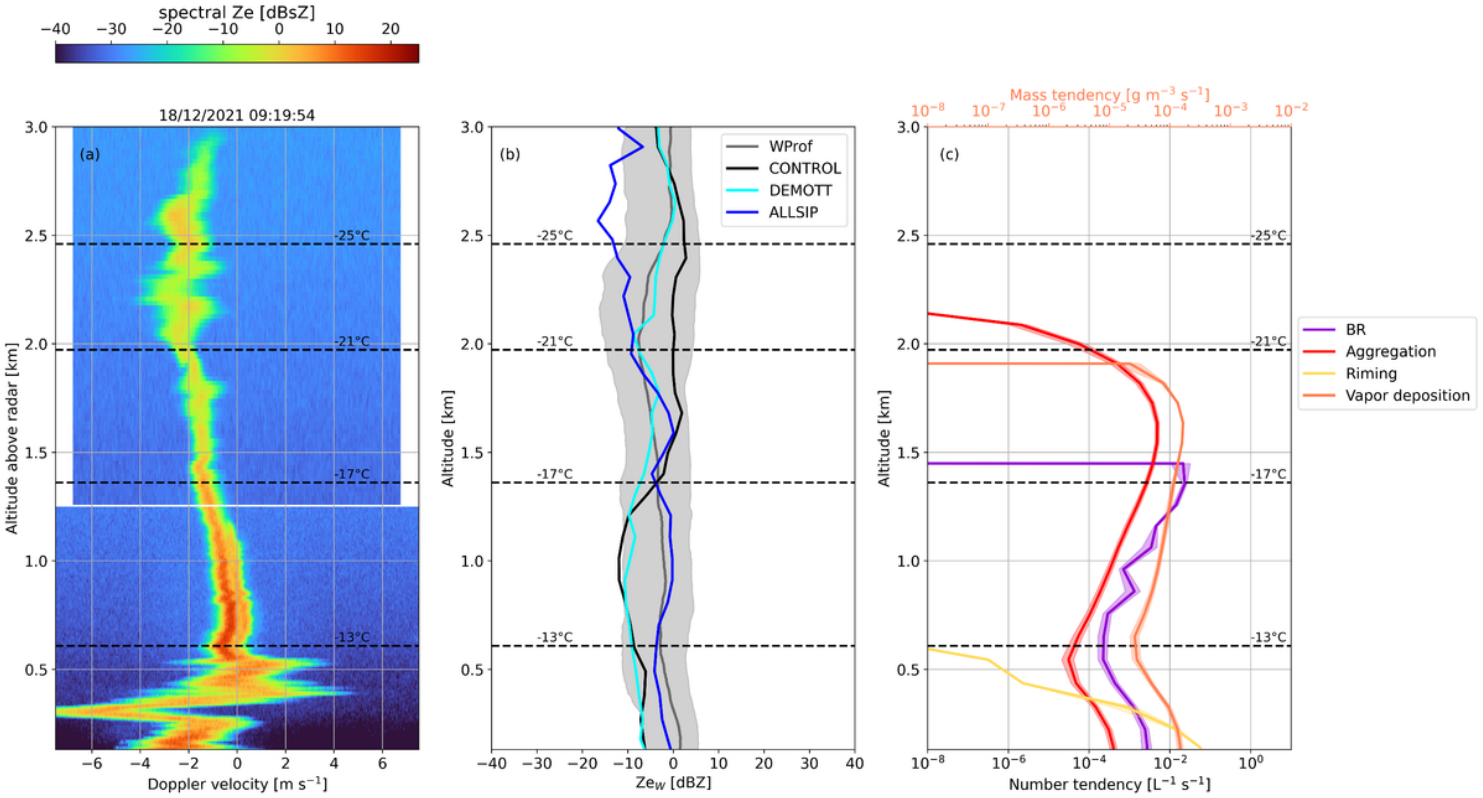

Figure 4

Synergistic insights from WProf radar Doppler spectra and WRF predictions: (a) Example of the WProf reflectivity spectrogram collected on December 18 at 03:55:10 UTC, during the nimbostratus cloud period. A horizontal white line around 1.2 km marks a sampling gap in a small radar volume between the first and second chirp. Note that 1dBsZ = $10\log_{10}$ (1mm^{6}m^{-3} (ms^{-1})$^{-1}$); (b) Median vertical profiles of observed and simulated radar reflectivity extracted during the nimbostratus cloud period. The grey line represents the median WProf observations, while the black, cyan, and blue lines denote the results from the CONTROL, DEMOTT, and ALLSIP simulations, respectively; (c) Median vertical profiles (extracted from the ALLSIP simulation over a 10-min time window centered around the chosen spectrogram) of the number tendency due to BR (purple line) and snow aggregation (red line) shown in the lower x-axis, while the mass tendencies due to riming (yellow) and vapor deposition (orange) are shown in the upper x-axis. The shaded regions correspond to the IQR, while the temperature contours superimposed in these panels are from the ALLSIP simulation. Note that the tendency due to snow aggregation in panel (c) is presented in absolute values.

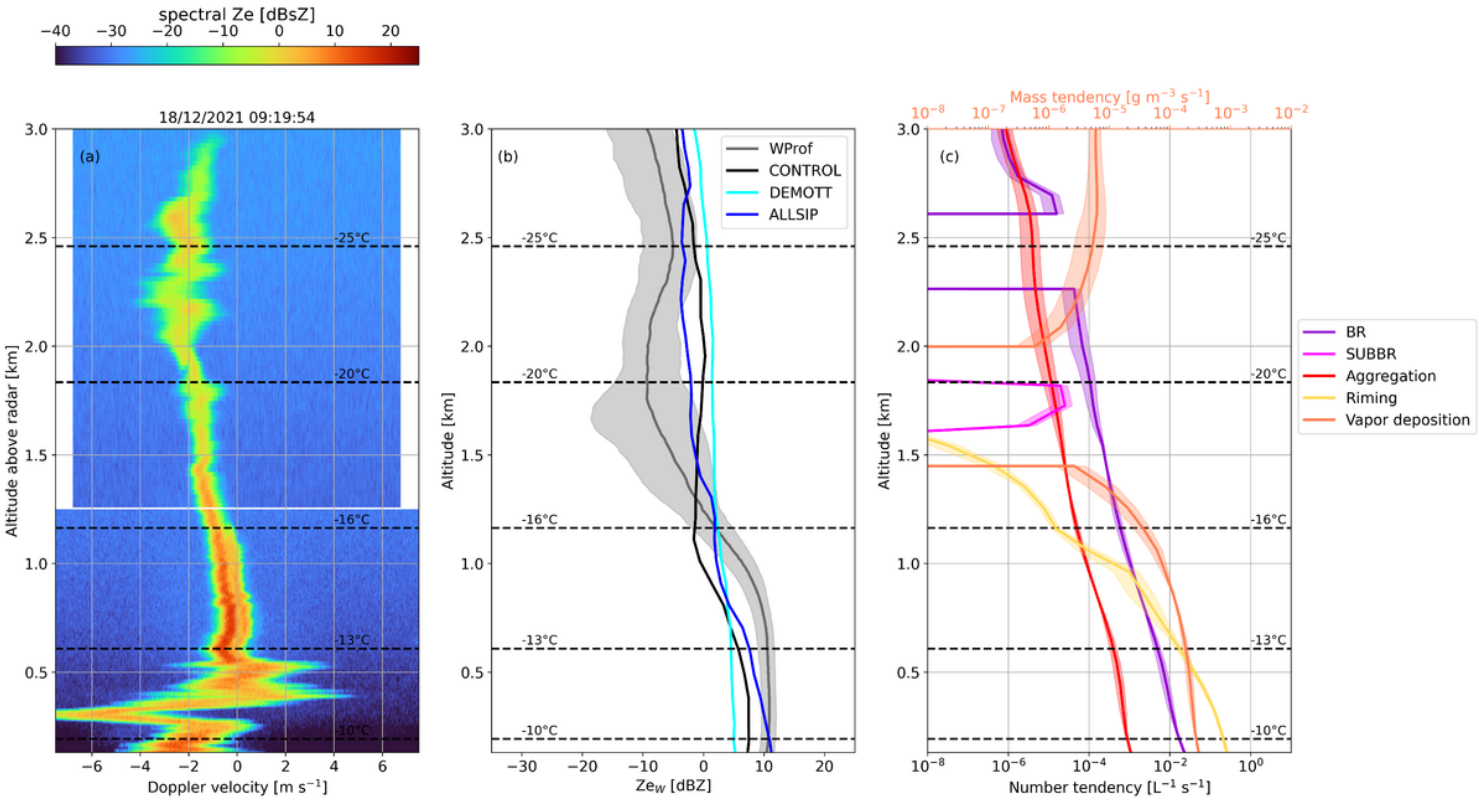

Figure 5

Same as in Fig. 4, but the information is extracted from December 18 at 09:19:54 UTC, during the seeder-feeder cloud period. In panel (c) the magenta line indicates the median vertical profile of the number tendency due to SUBBR shown in the lower x-axis.

Supplementary Files

This is a list of supplementary files associated with this preprint. Click to download.

- CarmelSInpjfinal.docx